Nonlinearity in the Dark: Broadband Terahertz Generation with Extremely High Efficiency

Ming Fang,[1,2] Nian-Hai Shen,[1,*] Wei E. I. Sha,[3] Zhixiang Huang,[2,†] Thomas Koschny,[1] and Costas M. Soukoulis[1,4]
[1]*Ames Laboratory—U.S. DOE and Department of Physics and Astronomy, Iowa State University, Ames, Iowa 50011, USA*
[2]*Key Laboratory of Intelligent Computing and Signal Processing, Ministry of Education, Anhui University, Hefei 230039, China*
[3]*Key Laboratory of Micro-nano Electronic Devices and Smart Systems of Zhejiang Province, College of Information Science and Electronic Engineering, Zhejiang University, Hangzhou 310027, China*
[4]*Institute of Electronic Structure and Lasers (IESL), FORTH, 71110 Heraklion, Crete, Greece*

(Received 18 July 2018; published 18 January 2019)

Plasmonic metamaterials and metasurfaces offer new opportunities in developing high performance terahertz emitters and detectors beyond the limitations of conventional nonlinear materials. However, simple meta-atoms for second-order nonlinear applications encounter fundamental trade-offs in the necessary symmetry breaking and local-field enhancement due to radiation damping that is inherent to the operating resonant mode and cannot be controlled separately. Here we present a novel concept that eliminates this restriction obstructing the improvement of terahertz generation efficiency in nonlinear metasurfaces based on metallic nanoresonators. This is achieved by combining a resonant dark-state metasurface, which locally drives nonlinear nanoresonators in the near field, with a specific spatial symmetry that enables destructive interference of the radiating linear moments of the nanoresonators, and perfect absorption via simultaneous electric and magnetic critical coupling of the pump radiation to the dark mode. Our proposal allows eliminating linear radiation damping, while maintaining constructive interference and effective radiation of the nonlinear components. We numerically demonstrate a giant second-order nonlinear susceptibility $\sim 10^{-11}$ m/V, a one order improvement compared with the previously reported split-ring-resonator metasurface, and correspondingly, a 2 orders of magnitude enhanced terahertz energy extraction should be expected with our configuration under the same conditions. Our study offers a paradigm of high efficiency tunable nonlinear metadevices and paves the way to revolutionary terahertz technologies and optoelectronic nanocircuitry.

DOI: 10.1103/PhysRevLett.122.027401

Following the emergence of quantum-cascade lasers [1–3] and ultrafast photoconductive switches [4], terahertz (THz) regime, a historically mysterious electromagnetic spectrum bridging microwaves and optics, in the past two decades has gained significant progress in technologies, leading to tremendous transformative applications in sensing, imaging, communication, etc. [4–9]. The blooming of THz technologies and related applications at the current stage demand urgently efficient and compact THz emitters and detectors, yet the development of which remains challenging. Many state-of-the-art THz sources are based on nonlinear optical rectification or difference-frequency generation (DFG) in inorganic crystals, which suffer from the drawbacks of narrow bandwidth, subtle phase-matching limitations, inevitable spectrum gaps, or low emission intensity [1–3,10–13]. Surpassing natural materials, the freedom of designing our own subwavelength-scale atoms as building blocks of metamaterials or metasurfaces has shown great flexibilities in achieving versatile functions in different disciplines [14–26]. The coexistence of resonant nonlinearity and local field enhancement in properly designed meta-atoms [23,27–32] opens up an alternative route for high-efficiency nonlinear devices that eliminates those common restrictions. Screening effects of the free-electron gas at the surface of metallic nanoparticles lead to strong second-order nonlinearity in their optical electric susceptibility, which contribute constructively in the area of the metasurface with the specifically designed non-symmetric shape of meta-atoms [33,34]. Very recently, a metasurface of 40 nm-thick split-ring resonators (SRRs) was demonstrated to generate broadband gapless THz emission (up to 4 THz) with the conversion efficiency close to 0.2 mm-thick optimal ZnTe crystals [35]. Despite of being a seminal progress toward compact tailorable THz sources even subwavelength all-optical active devices benefiting next generation computations and communications, the nonlinear optical response reported in Ref. [35] is still fairly weak. Therefore, a fundamental improvement in nonlinear efficiency with metasurface-based devices is critical.

In this Letter, we reveal a fundamental limit of conversion efficiency in nonlinear metasurfaces, and accordingly, we propose a dark-mode-assisted perfect absorbing metasurface for THz generation that allows us to circumvent it. We demonstrate broadband THz emissions of the metasurface with giant efficiency, about 2 orders stronger compared to that of a conventional SRR metasurface [35]. This opens up opportunities for not only revolutionary THz technologies but also high efficiency on-chip nonlinear nano-optical devices.

Analyzing the performance of the SRR metasurface we find that the major obstacles limiting the nonlinear conversion efficiency are dissipative and radiative damping due to linear scattering. These two loss channels essentially govern the amplitude of the local near field, which in turn reduces the possible THz emission intensity. For the second-order nonlinearity, the ratio of generated THz signal to scattered pump radiation is directly proportional to the local near-field amplitude, thus the linear radiation damping reduces the THz output. While the dissipative loss is hard to minimize and essentially given by the available constituent materials, we, therefore, target the radiative loss channel. Theoretically, we should be able to tackle these restrictions and approach the critical limit in the nonlinear efficiency of a metasurface: a properly designed *perfect absorbing* metasurface is applied to eliminate the linear radiative damping and a low-loss dielectric dark element can be introduced for high quality-factor strong local field enhancement to drive the plasmonic nanoparticles, which are generating the nonlinear signals.

In order to implement the concept, we tried to separate the resonant local field enhancement from the current topology necessary for nonvanishing second-order nonlinearity. Instead of driving the SRR directly, we used a resonant dark bound state in a silicon film with a subwavelength thickness to create local field enhancement and the strong evanescent surface fields of this quasisurface mode then drive the SRRs. The low-loss dielectric dark state allows us to concentrate significant amounts of electromagnetic field energy in the metasurface and to create a high Q factor with strong local field enhancement. Figure 1(a) presents the schematic unit of our designed metasurface THz emitter. Two gold SRRs (thickness t_m), oriented in the same direction, asymmetrically sit on the two sides of a thin Si slab (thickness h), which is periodically punctuated by metal walls (gold, width $2a$). The two SRRs are not only the key element for THz emission via DFG, but also serve as a bridge coupling the incident wave into the dark element (Si slab). The introduction of metal walls is to quantize the modes of the dielectric slab achieving a set of discrete resonant dark states [see Fig. 1(b)]. Depending on the branch of the dispersion, we may choose one desired mode frequency with the specific corresponding spatial distribution of the composite system for operation. Here, for simplicity, we select the second quantized mode on the lowest branch of dispersion for the dielectric slab, that is, the $\mathrm{TE}_{2,0}$ mode [marked by a red circle in Fig. 1(b)], which gives an antisymmetric profile of the electric field as shown in Fig. 1(a), a dark mode not being able to directly couple to the incident plane wave. The geometric parameters of the unit are designed to have the length $L = 800$ nm, width $W = 240$ nm, and thickness $h = 100$ nm, so the operation wavelength is tuned within the typical high-speed telecommunications range at around 1.5 μm. The thickness of the SRRs is set as $t_m = 50$ nm.

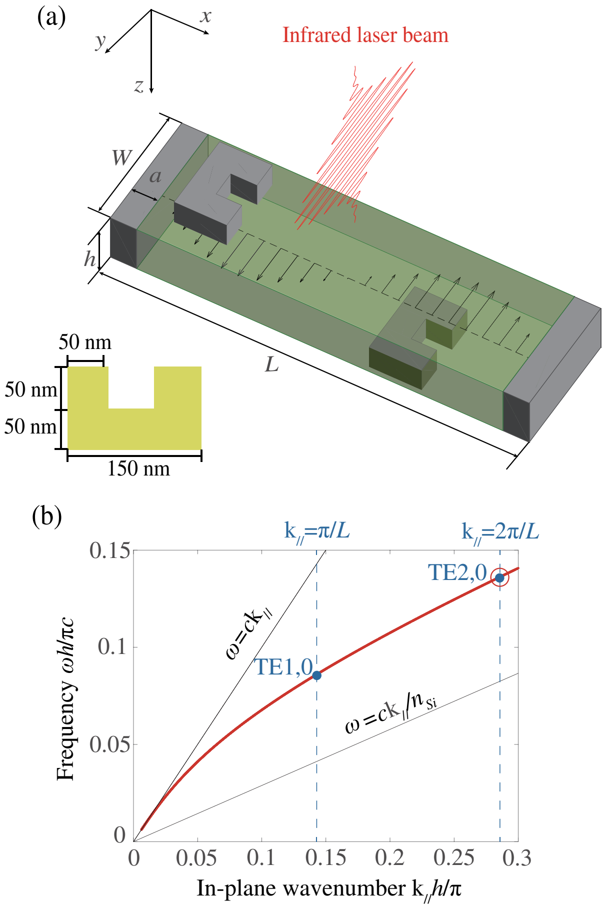

FIG. 1. Designed dark-mode THz emitter and principle of operation. (a) Schematics of the meta-atom of designed metasurface THz emitter. (b) Dispersion diagram of the system. The solid (red) line shows the lowest TE branch and vertical dashed (blue) lines indicate the quantization of eigenmodes. The blue dots are the quantized eigenstates of the lowest TE branch, and the red circle indicates the $\mathrm{TE}_{2,0}$ mode adopted in this work.

Coupling of the pump radiation to the resonant dark state can be achieved via the nonresonant weak SRR scatterers, which are designed to simultaneously couple both the electric and magnetic component of the pump to the resonant dark state by creating equivalent electric and magnetic effective surface susceptibilities in the metasurface. In-phase linear currents in the two SRRs created electric moments and antiphase linear currents in SRRs on opposing sides of the film created magnetic moments; the absolute and relative strength of both can be controlled by the symmetry and lateral positioning of the SRRs.

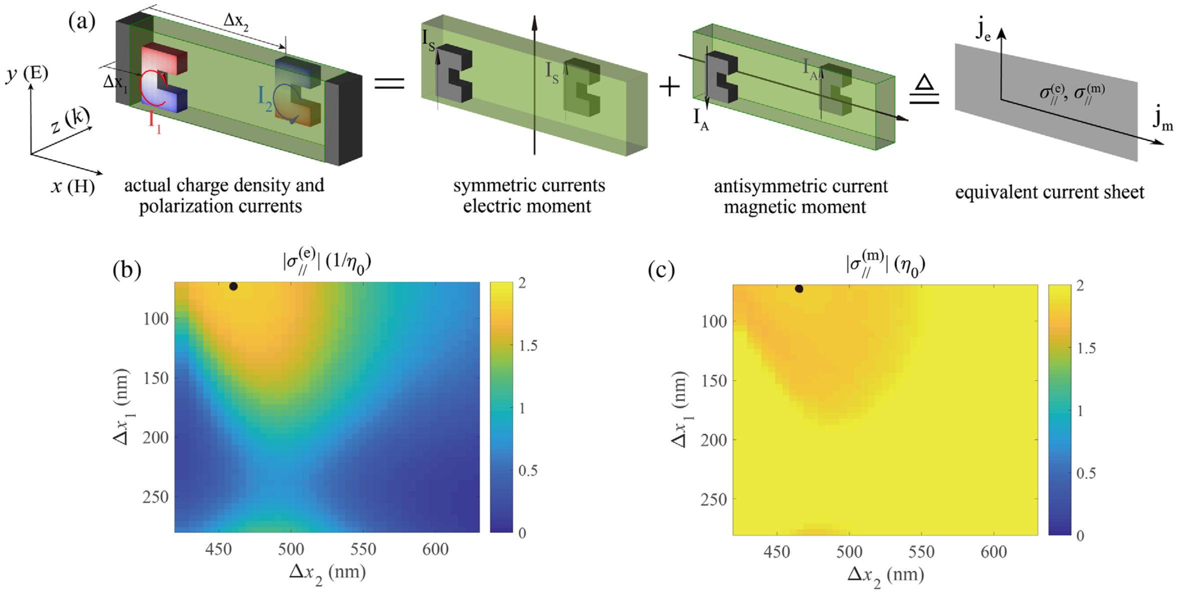

FIG. 2. Equivalent current sheet. (a) Polarization currents on two SRRs ($\mathbf{I}_1$ and $\mathbf{I}_2$) can be decomposed into the set of symmetric ($\mathbf{I}_S$) and antisymmetric ($\mathbf{I}_A$) currents, equivalently described by electric ($\sigma_s^{(e)}$) and magnetic ($\sigma_s^{(m)}$) sheet conductivities. (b),(c) Maps of $\sigma_s^{(e)}$ and $\sigma_s^{(m)}$ in dependence of positions of the two SRRs. Black dots indicate the optimized case of the system showing the highest absorption.

By shifting the positions of the two SRRs, i.e., Δx_1 and Δx_2, the energy of excitation exchanged to the dark state indeed can be controlled purposely. Upon the excitation of the TE$_{2,0}$ mode in the Si slab, out-of-phase polarization currents $\mathbf{I}_1$ and $\mathbf{I}_2$ are induced in the two SRRs, which can be decomposed to symmetric (corresponding to an electric moment along the y axis) and antisymmetric (corresponding to a magnetic moment along the x axis) polarization sets, respectively, as shown in Fig. 2(a). Balancing the electric and magnetic coupling allowed for impedance match, hence, eliminating the reflection of the pump energy. Tuning the coupling strength to a critical case also allowed us to further eliminate the linear transmitted field, thus leading to a complete channeling of the incident pump energy into the dark resonant state and dissipative loss in the metal structures. Consequently, the proposed metasurface can be characterized by the set of electric and magnetic sheet conductivities, i.e., $\sigma_s^{(e)}$ and $\sigma_s^{(m)}$, which are directly connected with the scattering properties, i.e., reflection, R and transmission, T, of the metasurface in expressions of: $R = 2(\zeta\sigma_s^{(e)} - \zeta^{-1}\sigma_s^{(m)})/(4 + 2\zeta\sigma_s^{(e)} + 2\zeta^{-1}\sigma_s^{(m)} + \sigma_s^{(e)}\sigma_s^{(m)})$ and $T = (4 - \sigma_s^{(e)}\sigma_s^{(m)})/(4 + 2\zeta\sigma_s^{(e)} + 2\zeta^{-1}\sigma_s^{(m)} + \sigma_s^{(e)}\sigma_s^{(m)})$, where ζ is the wave impedance [36]. An ideal perfect absorbing sheet should fulfill the condition $\zeta\sigma_s^{(e)} = \zeta^{-1}\sigma_s^{(m)} = 2$. For our design, we calculated the sheet conductivities in the dependence of (Δx_1, Δx_2) with a scanning step size of 5 nm, balancing the simulation resolution and cost. The results are shown in Figs. 2(b) and 2(c), from which, the optimal case may be picked at $\Delta x_1 \cong 70$ nm and $\Delta x_2 \cong 470$ nm with $\zeta|\sigma_s^{(e)}| = \zeta^{-1}|\sigma_s^{(m)}| = 1.8$ and the corresponding absorption reaches as high as 94% (see below in Fig. 3).

Depending on the relative positions of the two SRRs, tunable linear radiation damping can be achieved as shown

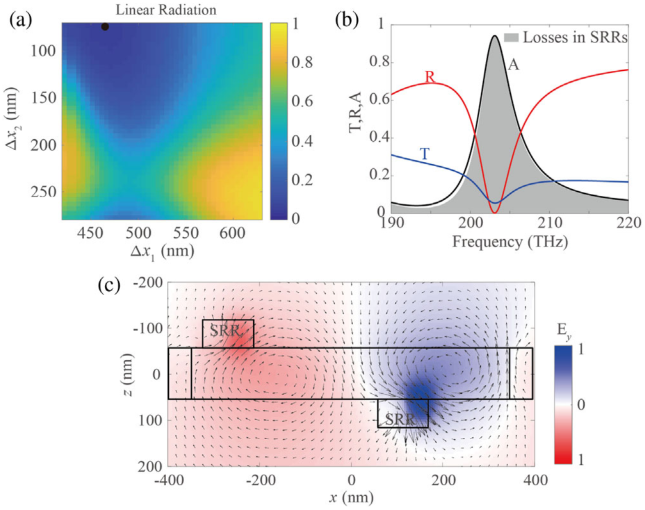

FIG. 3. Scattering properties of the metasurface. (a) Normalized linear radiation damping as each scatterer is shifted along the unit cell, black dots indicate the optimized case. (b) Transmission, reflection, and absorption spectra for the optimized metasurface. The gray-shaded region shows the dissipation in two SRRs. (c) Color plot shows the y component of the electric field, E_y, and black arrows indicate the magnetic field, $\mathbf{H}$, in the x-z plane across the center of the meta-atom.

in Fig. 3(a). For the optimized configuration with *nearly perfect absorption*, Fig. 3(b) presents the calculated transmission (T), reflection (R), and absorption (A) spectra for the optimized configuration, with the shaded area indicating the dissipation in the two SRRs. In Fig. 3(c), we show the field distributions, i.e., the y component of the electric field, E_y, indicated in color and the magnetic field, $\mathbf{H}$, marked with black arrows, in the x-z plane perpendicularly across the center of the Si slab at $y = 0$. From Fig. 3(c) we see that the high quality-factor $\mathrm{TE}_{2,0}$ mode of the Si slab is strongly excited, featuring an antisymmetric electric field profile, leading to dramatic field enhancement around SRRs. Considering the metal walls always coincide with a field minimum of the dark mode, most of the incident energy will be dissipated in SRRs and converted to nonlinear signals. We need to point out that the dimensions of the SRRs are not critical, provided that the requirements of proper dark-mode frequency and perfect absorption for eliminating the linear radiation are fulfilled.

For the nonlinear process, THz radiation, we can choose to re-use the two SRRs, which are necessary anyway for providing nonlinearity. Since the desired DFGs (or also second-harmonic generation) are second order in the electric filed $\mathbf{E}$, the sign of the currents does not matter and the nonlinear radiation of both SRRs adds constructively in the far field. The linear radiation, however, is opposite in phase and cancels in the far field, thus completely eliminating linear radiation damping. Since radiation damping of the scattered linear fields, after local dissipation, is the second biggest loss channel in the conversion of pump energy to THz radiation via DFG, this cancellation can significantly increase the efficiency. Consequently, the two SRRs, driven by the $\mathrm{TE}_{2,0}$ mode of the slab, show the same second-order nonlinear dynamic but opposite linear electric and magnetic dipole moments, resulting in linear radiation cancellation and significant enhancement of THz radiation. By illuminating the designed metasurface with a laser pulse at the resonant frequency of the dark mode, strong THz emission from the SRRs will be observed due to DFG arising from the electron gas in the metal of the SRRs, which can be described by the hydrodynamic model [33,34] (see Supplemental Material [37] for details). In the model, the convection term plays the crucial role for the second-order nonlinearities, qualitatively contributing in the format as the product of current and accumulated charge density on the metal surface.

For a rigorous analysis of THz radiation from the metasurface, we performed a self-consistent finite-difference time-domain (FDTD) calculation based on the hydrodynamic model and Maxwells equations (see Supplemental Material [37]). A temporal optical pulse was applied, $E_y(t) = E_0 \exp[-2\ln(2)(t - t_0)^2/\tau^2]\cos(\omega_0 t)$, where the driving frequency equals the resonant frequency of the dark mode, i.e., $\omega_0 = \omega_{\mathrm{dark}}$, the pulse duration $\tau = 140$ fs (spectral width $\sim$3.2 THz), and peak amplitude $E_0 = 2 \times 10^7$ V/m (see Supplemental Material [37] for our estimation to thermal damage threshold of the metasurface). In our calculations, both the linear and nonlinear dynamics of the electron gas under the infrared light excitation have been fully considered. In Fig. 4(a), we show a performance map of our proposed THz emitter in terms of THz enhancement defined as $\eta_{\mathrm{dark}}/\eta_{\mathrm{SRR}}$, where η_{dark} and η_{SRR} represent the THz conversion efficiency of our system and that of the traditional SRR metasurface [35] (as a reference), respectively. By properly settling the two SRRs, we can significantly eliminate the radiation damping, resulting in more than 120-fold enhancement in THz emission power compared to the reference case. Note that the THz enhancements for different configurations are inversely proportional to the linear radiation damping as shown in Fig. 4(a). Figure 4(b) gives the typical time-domain trace detected at the receiving port for our metasurface THz emitter compared to that for the reference SRR case. Upon increasing the pump pulse intensity, the generated THz signal amplitude increases linearly as presented in Fig. 4(c), and our design does show a dramatic emission enhancement over the analog dependence for the conventional SRR metasurface under the same conditions. In Fig. 4(d), we illustrate the charge density distribution (marked in color) and the currents (indicated with arrows) in the two SRRs at the maximum THz conversion efficiency. Both SRRs, possessing the same

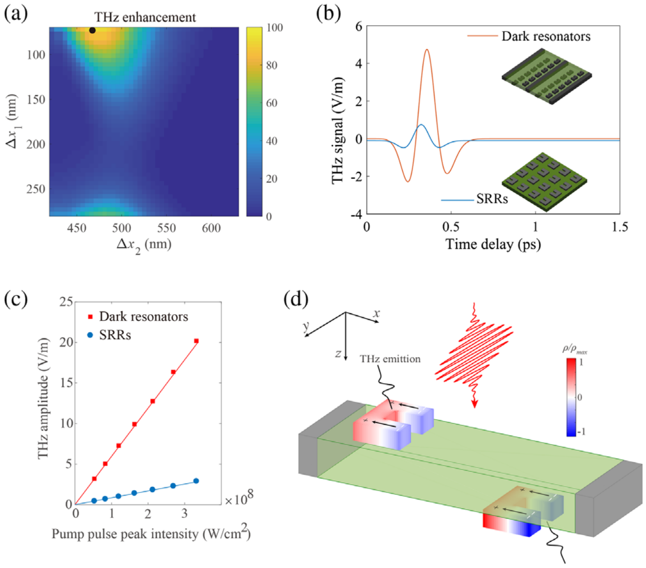

FIG. 4. Terahertz enhancement of our design. (a) THz intensity enhancement map of our design. (b) Time trace of THz radiation from design (red) compared to that from traditional SRR metasurface (blue). (c) Terahertz signal strength in dependence of pump power for our design (red squares) and for traditional SRRs (blue dots). The straight lines are from linear fitting. (d) Distributions of DFG currents (black arrows) and charge density (color plot) of the SRRs. "+" and "−" indicate charge accumulations.

polarization with negligible phase difference, contribute to the THz emission (polarized along the x axis) coherently, the superposition of which leads to the total enhanced THz radiation, emitting perpendicular to the metasurface on both sides (see Supplemental Material [37]). Moreover, the radiated THz signal polarized in the x direction can be written in terms of second-order nonlinear susceptibility $\chi^{(2)}$ of the metasurface as $E_x^{\mathrm{THz}}(\omega) \sim \chi^{(2)}\omega^2 e^{-\omega^2\tau^2} \Rightarrow E_x^{\mathrm{THz}}(t) \sim \chi^{(2)}(1-2t^2/\tau^2)e^{-t^2/\tau^2}/\tau^2$.

The THz signal depends on the temporal envelope of the incident pulse, and THz spectrum has the peak at $\omega = 2/\tau$ with a bandwidth $\Delta\omega_{\mathrm{FWHM}} \approx 2.31/\tau$. From the field of second harmonic radiation, we evaluated the effective nonlinear susceptibility of our designed metasurface $\chi^{(2)}_{\mathrm{dark}} \approx 2.4 \times 10^{-11}$ m/V, while that of the traditional SRR metasurface $\chi^{(2)}_{\mathrm{SRR}} \approx 1.7 \times 10^{-12}$ m/V (consistent with the reported 1.6×10^{-12} m/V in Ref. [35]). The discussions of the case with a substrate can be found in the Supplemental Material [37]. In the view of potential experiments, conversion efficiency is an important parameter for an intuitive evaluation on nonlinear energy extraction. In practice, for a specific experimental setup, it depends on many factors, such as pump power, pump polarization, pulse duration, incidence and focusing conditions, phase matching, etc. Our theoretical work described here resolves a fundamental problem obstructing the improvement of THz generation efficiency with nonlinear metasurfaces, and to understand the fundamental physics, we considered a simplified model of a spatially infinite surface under plane-wave illumination, so the model is less suitable to predict practical absolute numbers as would be observed in a particular experiment. Therefore, we conducted a side-by-side comparison between the conventional, not radiation-managed SRR metasurface [35], for which experimental data are available, and our configuration, which eliminates linear radiation damping, within the same numerical simulations. It is revealed that our scheme has $\chi^{(2)}$ more than one order of magnitude larger than that of the regular SRR metasurface, and consequently would generate over 2-order enhanced THz emission under the same conditions. On the other hand, Ref. [35] reported that the SRR metasurface experimentally showed about the same order of THz generation as a 0.2 mm-thick ZnTe crystal, so our proposed configuration should show a much better performance in generating broadband THz emission in real experiments.

In conclusion, our proposed system demonstrates effective suppression of radiation damping and extremely high-efficiency THz generations with a specifically designed metasurface. Such significant improvements in nonlinear conversion efficiency were made possible by our judiciously designed dark-element-integrated perfect absorbing sheet, which essentially tackled the common efficiency limit in two crucial aspects, i.e., eliminating radiative damping of linear scatterings and enhancing the local field for nonlinear signals. Although our design presented in this Letter aims for efficient and compact THz generations, the new concept is general and applicable to other nonlinear processes. We believe the flexibilities in tailoring meta-atoms of metamaterials, especially metasurfaces, will open up new opportunities for THz technologies development and versatile nanoscale nonlinear devices.

Work at Ames Laboratory was supported by the US Department of Energy, Office of Basic Energy Science, Division of Materials Science and Engineering (Ames Laboratory is operated for the US Department of Energy by Iowa State University under Contract No. DE-AC02-07CH11358). Work at FORTH was supported by the European Research Council under the ERC Advanced Grant No. 320081 (PHOTOMETA). The work was also supported by NSFC (No. 61601166, No. 61701001, No. 61701003), National Natural Science Fund for Excellent Young Scholars (No. 61722101), Universities Natural Science Foundation of Anhui Province (No. KJ2017ZD51 and No. KJ2017ZD02), and Thousand Talents Program for Distinguished Young Scholars of China. The authors would like to thank Peng Zhang, Liang Luo, and Xu Yang for fruitful discussions.

---

[*] nhshen@ameslab.gov
[†] zxhuang@ahu.edu.cn

[1] R. Köhler, A. Tredicucci, F. Beltram, H. E. Beere, E. H. Linfield, A. G. Davies, D. A. Ritchie, R. C. Iotti, and F. Rossi, Nature (London) **417**, 156 (2002).
[2] B. S. Williams, Nat. Photonics **1**, 517 (2007).
[3] G. Scalari, C. Walther, M. Fischer, R. Terazzi, H. Beere, D. Ritchie, and J. Faist, Laser Photonics Rev. **3**, 45 (2009).
[4] M. Tonouchi, Nat. Photonics **1**, 97 (2007).
[5] D. M. Mittleman, *Sensing with Terahertz Radiation*, Vol. 85 (Springer Berlin Heidelberg, Berlin, Heidelberg, 2003).
[6] H. J. Song and T. Nagatsuma, IEEE Trans. Terahertz Sci. Technol. **1**, 256 (2011).
[7] P. Siegel, IEEE Trans. Microwave Theory Tech. **50**, 910 (2002).
[8] C. Jansen, S. Wietzke, O. Peters, M. Scheller, N. Vieweg, M. Salhi, N. Krumbholz, C. Jördens, T. Hochrein, and M. Koch, Appl. Opt. **49**, E48 (2010).
[9] J. Federici and L. Moeller, J. Appl. Phys. **107**, 111101 (2010).
[10] R. A. Lewis, J. Phys. D **47**, 374001 (2014).
[11] B. Ferguson and X. C. Zhang, Nat. Mater. **1**, 26 (2002).
[12] M. A. Belkin, F. Capasso, A. Belyanin, D. L. Sivco, A. Y. Cho, D. C. Oakley, C. J. Vineis, and G. W. Turner, Nat. Photonics **1**, 288 (2007).
[13] Z. Yang, L. Mutter, M. Stillhart, B. Ruiz, S. Aravazhi, M. Jazbinsek, A. Schneider, V. Gramlich, and P. Günter, Adv. Funct. Mater. **17**, 2018 (2007).
[14] N. Engheta, Science **317**, 1698 (2007).
[15] C. M. Soukoulis and M. Wegener, Nat. Photonics **5**, 523 (2011).

[16] A. F. Koenderink, A. Alù, and A. Polman, Science **348**, 516 (2015).
[17] H. T. Chen, A. J. Taylor, and N. Yu, Rep. Prog. Phys. **79**, 076401 (2016).
[18] N. K. Grady, J. E. Heyes, D. R. Chowdhury, Y. Zeng, M. T. Reiten, A. K. Azad, A. J. Taylor, D. A. Dalvit, and H. T. Chen, Science **340**, 1304 (2013).
[19] V. G. Kravets, F. Schedin, R. Jalil, L. Britnell, R. V. Gorbachev, D. Ansell, B. Thackray, K. S. Novoselov, A. K. Geim, A. V. Kabashin, and A. N. Grigorenko, Nat. Mater. **12**, 304 (2013).
[20] N. Meinzer, W. L. Barnes, and I. R. Hooper, Nat. Photonics **8**, 889 (2014).
[21] A. V. Kildishev, A. Boltasseva, and V. M. Shalaev, Science **339**, 1232009 (2013).
[22] N. Yu, P. Genevet, M. A. Kats, F. Aieta, J.-P. Tetienne, F. Capasso, and Z. Gaburro, Science **334**, 333 (2011).
[23] A. E. Minovich, A. E. Miroshnichenko, A. Y. Bykov, T. V. Murzina, D. N. Neshev, and Y. S. Kivshar, Laser Photonics Rev. **9**, 195 (2015).
[24] N. I. Zheludev and Y. S. Kivshar, Nat. Mater. **11**, 917 (2012).
[25] A. Baev, P. N. Prasad, H. Ågren, M. Samoć, and M. Wegener, Phys. Rep. **594**, 1 (2015).
[26] N. Yu and F. Capasso, Nat. Mater. **13**, 139 (2014).
[27] S. Linden, F. B. P. Niesler, J. Förstner, Y. Grynko, T. Meier, and M. Wegener, Phys. Rev. Lett. **109**, 015502 (2012).
[28] P. Ginzburg, A. Krasavin, Y. Sonnefraud, A. Murphy, R. J. Pollard, S. A. Maier, and A. V. Zayats, Phys. Rev. B **86**, 085422 (2012).
[29] M. Lapine, I. V. Shadrivov, and Y. S. Kivshar, Rev. Mod. Phys. **86**, 1093 (2014).
[30] H. Husu, R. Siikanen, J. Mäkitalo, J. Lehtolahti, J. Laukkanen, M. Kuittinen, and M. Kauranen, Nano Lett. **12**, 673 (2012).
[31] O. Wolf, S. Campione, A. Benz, A. P. Ravikumar, S. Liu, T. S. Luk, E. A. Kadlec, E. A. Shaner, J. F. Klem, M. B. Sinclair, and I. Brener, Nat. Commun. **6**, 7667 (2015).
[32] M. Kauranen and A. V. Zayats, Nat. Photonics **6**, 737 (2012).
[33] C. Ciracì, E. Poutrina, M. Scalora, and D. R. Smith, Phys. Rev. B **85**, 201403 (2012).
[34] Y. Zeng, W. Hoyer, J. Liu, S. W. Koch, and J. V. Moloney, Phys. Rev. B **79**, 235109 (2009).
[35] L. Luo, I. Chatzakis, J. Wang, F. B. P. Niesler, M. Wegener, T. Koschny, and C. M. Soukoulis, Nat. Commun. **5**, 3055 (2014).
[36] P. Tassin, T. Koschny, and C. M. Soukoulis, Physica B (Amsterdam) **407**, 4062 (2012).
[37] See Supplemental Material at http://link.aps.org/supplemental/10.1103/PhysRevLett.122.027401 for details on FDTD simulations of nonlinear dynamics in plasmonic metasurface, estimation of the thermal damage threshold on the design, the case of the metasurface with substrate and the discussion of polarization of the generated THz signals.

Supplemental Material

Nonlinearity in the dark: Broadband terahertz generation with extremely high efficiency

Ming Fang[1,2], Nian-Hai Shen[1,*], Wei EI Sha[3], Zhixiang Huang[2,†], Thomas Koschny[1], Costas M. Soukoulis[1,4]

[1] Ames Laboratory—U.S. DOE and Department of Physics and Astronomy and, Iowa State University, Ames, Iowa 50011, USA

[2] Key Laboratory of Intelligent Computing and Signal Processing, Ministry of Education, Anhui University, Hefei 230039, China

[3] Key Laboratory of Micro-nano Electronic Devices and Smart Systems of Zhejiang Province, College of Information Science and Electronic Engineering, Zhejiang University, Hangzhou 310027, China.

[4] Institute of Electronic Structure and Lasers (IESL), FORTH, 71110 Heraklion, Crete, Greece

(*email: nhshen@ameslab.gov, † email: zxhuang@ahu.edu.cn)

I. FDTD simulations of nonlinear dynamics in plasmonic metasurface

The interaction of electromagnetic fields **E** and **H** with metal can be described by the Maxwell's equations and hydrodynamic model.

$$\nabla\times\mathbf{H}=\varepsilon_0\frac{\partial\mathbf{E}}{\partial t}+\frac{\partial\mathbf{P}}{\partial t}, \tag{S1}$$

$$\nabla\times\mathbf{E}=-\mu_0\frac{\partial\mathbf{H}}{\partial t}, \tag{S2}$$

$$\frac{\partial\mathbf{v}}{\partial t}+\mathbf{v}\cdot\nabla\mathbf{v}=-\frac{e}{m}(\mathbf{E}+\mu_0\mathbf{v}\times\mathbf{H})-\gamma\mathbf{v}-\frac{\nabla p}{n}, \tag{S3}$$

$$\frac{\partial n}{\partial t}=-\nabla\cdot(n\mathbf{v}). \tag{S4}$$

where ε_0, μ_0, m, e, and γ are the vacuum permittivity, vacuum permeability, electron mass, electron charge and electron collision rate, respectively. $n(\mathbf{r},t)$ and $\mathbf{v}(\mathbf{r},t)$ are the time- and position-dependent electron density and velocity. Term p in Eq.(S3) is the electron pressure and evaluated by the Thomas-Fermi model $p=(3\pi^2)^{2/3}(\hbar/5)n^{5/3}$. The polarization **P** of materials in Eq.(S1) relates to the hydrodynamic variables by $\dot{\mathbf{P}}=\mathbf{J}=-en\mathbf{v}$.

Equations (S1)-(S4) provide a self-consistent description of the electron gas in metal. For a numerical analysis of nonlinear response in metal, the multi-physics model set of Eqs. (S1)-(S4) was implemented with the help of the FDTD method. To numerically model the transient problem in the plasmonic systems, we used the Yee grids to maintain charge conservation and divergence-free condition (see Fig. S1). The electric field **E** and electron density n are defined at the time step l+1/2 and are respectively located at the grid face center and grid center, respectively. The velocity **v** and magnetic field **H** are defined at the time step l and located at the grid face center and the grid edges, respectively. With the central difference discretization used for solving Eqs. (S1)-(S4) for **E**, **H**, **v**, and n components using the explicit time-stepping scheme.

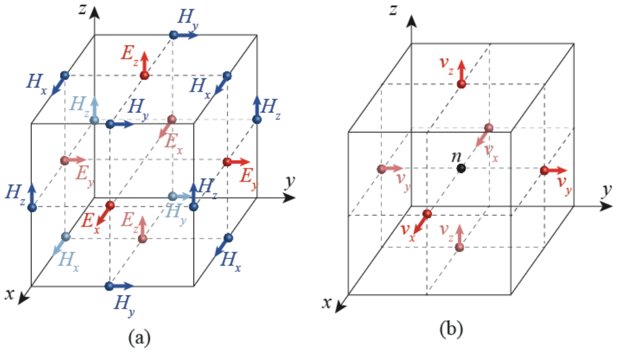

Figure S1: The Yee grids for the Maxwell-hydrodynamic system. (a) Maxwell's equations. (b) Hydrodynamic equations.

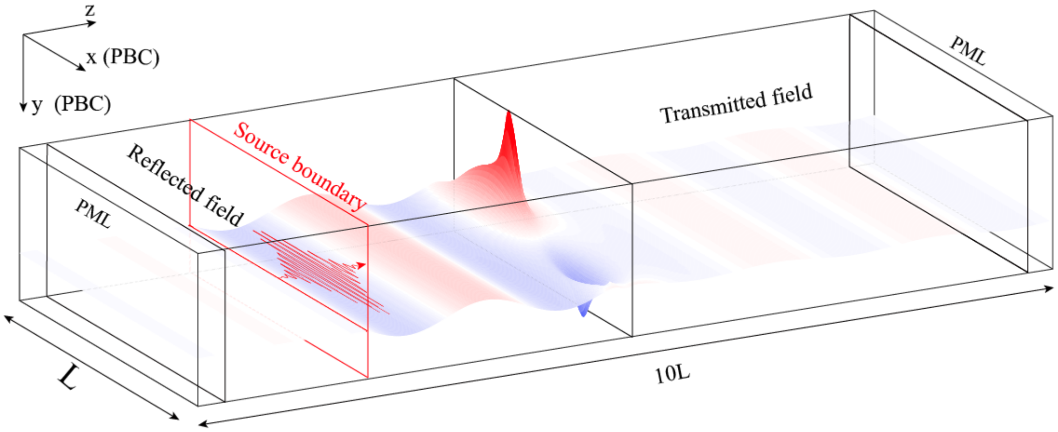

Figure S2: Layout of the time-domain numerical simulations. Snapshot of the electric field during the simulation. The central position along z-direction of the unit cell is marked with black lines in the framing. Electric fields in the reflected field region and transmitted total field are close to zero for the optimized metasurface and most of the linear power is trapped in the dark mode.

Parameters for gold SRRs are chosen as $n_0 = 5.92\times10^{28}$ m^{-3}, $\gamma = 13.05\times10^{12}$ rad/s. An x-polarized infrared laser pulse propagating in the z-direction is introduced by using the total-field and scattered-field (TF/SF) technique. Perfectly matched layers (PMLs) are applied in the z-direction and periodic boundaries are employed in both the x- and y- directions. Uniform spatial steps $\Delta x = \Delta y = \Delta z = 5$ nm and time step $\Delta t = 7.5\times10^{-18}$ s are used in the simulations. The perspective view of the simulation domain is shown in Fig. S2, the surface plot shows a temporal electric field distribution during the simulation.

II. Estimation of thermal damage threshold on the design

We performed a series of rough estimations on the thermal damage threshold of our design in a typical experimental setup comparable in Ref. [35]. Let us assume an experimentally realistic pump laser with a pump fluence of 100 μJ/cm^2 per pulse at the surface of our configuration (this is on the large side of commonly applied pump powers for related studies) with a pulse duration 140 fs at a repetition rate of 1 kHz. First, we considered the instantaneous heating of the SRR nanostructures in our design by a single laser pulse. Each pump pulse deposits about 100 fJ of energy per SRR of the metasurface. Assuming that ALL the energy of the pump pulse gets absorbed ONLY into the SRRs and distributed homogeneously through the just 40 nm thick nanoparticle, then applying the values of heat capacity (C), density of gold (ρ) and calculated volume (V) of SRRs to the heat capacity formula ($C\rho V\Delta T = Q$), we can obtain an upper bound for the instantaneous increase of temperature of the SRRs of about 62 K. From this low temperature increase, we conclude that the designed structure should NOT be damaged instantaneously. Next, the repeatedly arriving laser pulses every 1 ms keep heating the SRRs with an average power of 100 mW per cm^2 (100 pW per SRR). The SRRs will simultaneously transfer heat to the ambient via thermal conduction to substrate and fixture as well as convective and radiative cooling from all the surfaces of the sample. Over time, the sample will reach a stationary temperature. In equilibrium, the incident power of 100 mW per illuminated cm^2 of the sample surface has to be dissipated by the sum of radiation and convection from the sample twice that surface (front and back surface) of the sample. Neglecting heat conduction to the fixture, we can approximate the dissipated power as function of the sample surface temperature by $P = \varepsilon\sigma A(T_{surface}^4 - T_{amb}^4) + R_\theta^{-1}(T_{surface} - T_{amb})$, where the first term comes from radiation and the last term from convective cooling. Using as a rough estimate the well-known thermal resistance (case to still air) of a ~3cm^2 surface area TO220 electronic component package of about 70 K/W, we estimate for our sample surface of ~2 cm^2 (front & back, natural convection) a thermal resistance of about R_θ~ 100 K/W. With $\varepsilon\sigma A \approx 0.8 \cdot 2\ \mathrm{cm}^2 \cdot 5.67\times10^{-8}\ \mathrm{W/(m^2\,K^4)} \approx 9.1 \times 10^{-12}\ \mathrm{W/K^4}$ we then estimate an equilibrium heat dissipation $P \approx 10^{-3}\ \mathrm{W/K} \cdot \Delta T + o(\Delta T/300\mathrm{K})^2 + 10^{-2}\ \mathrm{W/K} \cdot \Delta T$, where the first two terms are from radiative cooling, the last from still air convection. Hence, for 100 mW incident power we expect an average sample temperature raise of ~10 K over ambient, overlaid with periodic ~60 K spikes every millisecond. This is an insignificant temperature raise that will not threaten the stability of the gold SRR, the adhesion of the metals, or the substrate of the metasurface in any way. We also would like to add, that this result compares favorably with the observed absence of any thermal damage to the sample in our previous experiments with the SRR metasurface from Ref. [35] at fluences exceeding 100 μJ/cm^2. With these numbers, the metasurface should be able to tolerate pump fluencies of at least one magnitude higher, i.e., ~ 1 mJ/cm^2 at 1 kHz repetition rate.

III. The case of the metasurface with substrate

For simplicity, the calculations and discussions in the main text part of the Letter were for a free-standing configuration. Here, we conducted additional simulations for the metasurface with a low-index SiO_2 substrate. Figure S3 shows the dispersion diagram of our THz emitter with SiO_2 substrate in comparison to the free-standing case. From Fig. S3, we can see that the introduction of the substrate would only lead to a slight frequency shift for the selected dark mode $TE_{2,0}$ of the Si slab from 204.3 THz of free-standing case to 199.05 THz, while the highest linear absorption still reaches 94.7% (see inset of Fig. R2). On the other hand, due to the effect of the substrate, the relative positions of the SRR pair in our scheme, i.e., (Δx_1, Δx_2), need to be adjusted slightly from (70 nm, 470 nm) to (60 nm, 490 nm) to account for the additional electric effective sheet currents due to the polarizability of the substrate. Figs. S4(a) and (b) show the operation frequency with respect to positions of SRRs for both cases of with and without the substrate, respectively. In Fig. S5, we show the calculated nonlinear signal in time domain (a) and second-order nonlinear spectra (b), respectively, for the cases of our proposed scheme with and without substrate, and regular SRR metasurface as well for comparison. We find the susceptibility $\chi^{(2)}$ of our design settled on a low-index substrate will be on the same order of magnitude as that of the free-standing case. Therefore, the introduction of some substrate in reality will NOT negatively impact the performance; only the geometric parameters need to be adjusted and the operation frequency will shift to some extent accordingly.

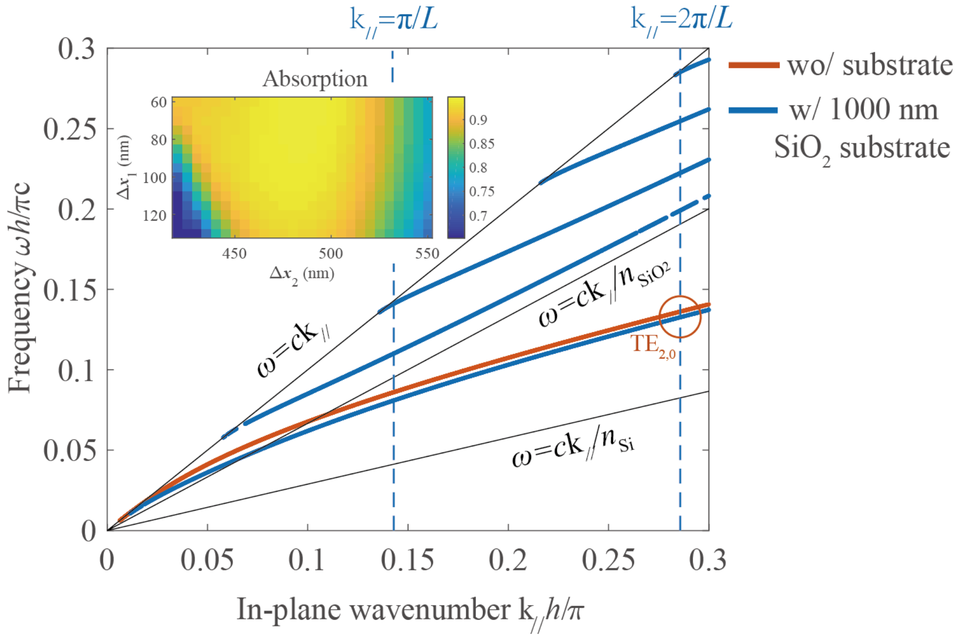

Figure S3: The dispersion diagram of our THz emitter with and without SiO2 substrate. The inset shows the normalized linear absorption for the case with substrate.

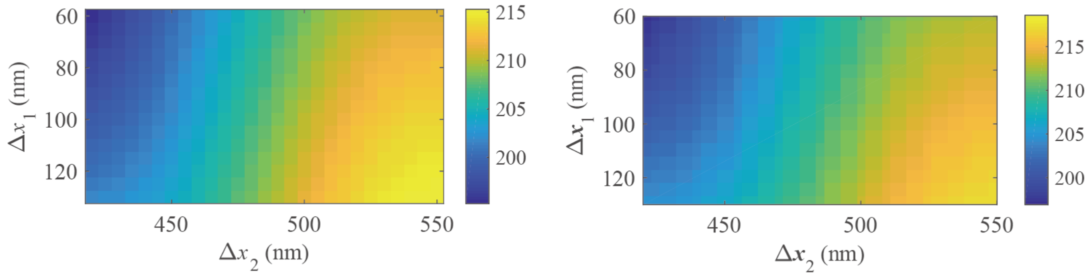

(a) (b)

Figure S4: The operation frequency for the case with the SiO_2 substrate (a) and the free-standing case (b).

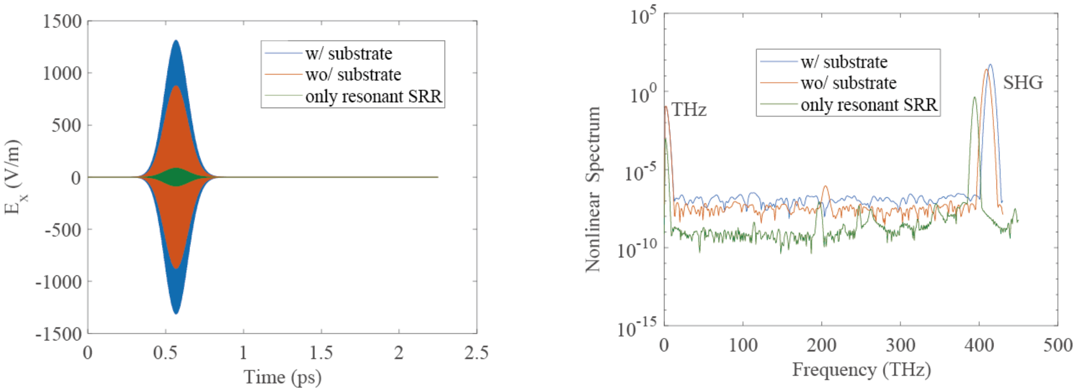

(a) (b)

Figure S5. The nonlinear signal in the time domain (a) and the second-order nonlinear spectra (b) for our configuration with and without SiO2 substrate in comparison to regular SRR metasurface.

IV. Polarization of the generated THz signals

The observed THz emission from the SRR is due to optical rectification arising from the electrons in the metal. As shown in Refs. [33-34], the electron gas in a metal can be described by the hydrodynamic model and the main nonlinear responses come from the convective acceleration, which does not contribute in the bulk but does contribute on surfaces, and qualitatively behaves like $j\rho$, where j is linear current and ρ accumulated charge density on the surface. As a consequence, the nonlinear current is parallel or antiparallel to the linear current induced by the external excitation in regions of increasing or decreasing surface charge, respectively. In our design with two SRRs driven by the out-of-phase field induced by the dark state (see Fig. S6), the linear responses (200 THz) of the two SRRs are opposite and get cancelled, while the nonlinear responses of the two SRRs are in phase and interfere constructively. The dielectric slab (Si) has a thickness of 100 nm, deeply subwavelength at the generated THz frequency. Therefore, the THz radiation from the SRRs has negligible phase delay and will be coherent.

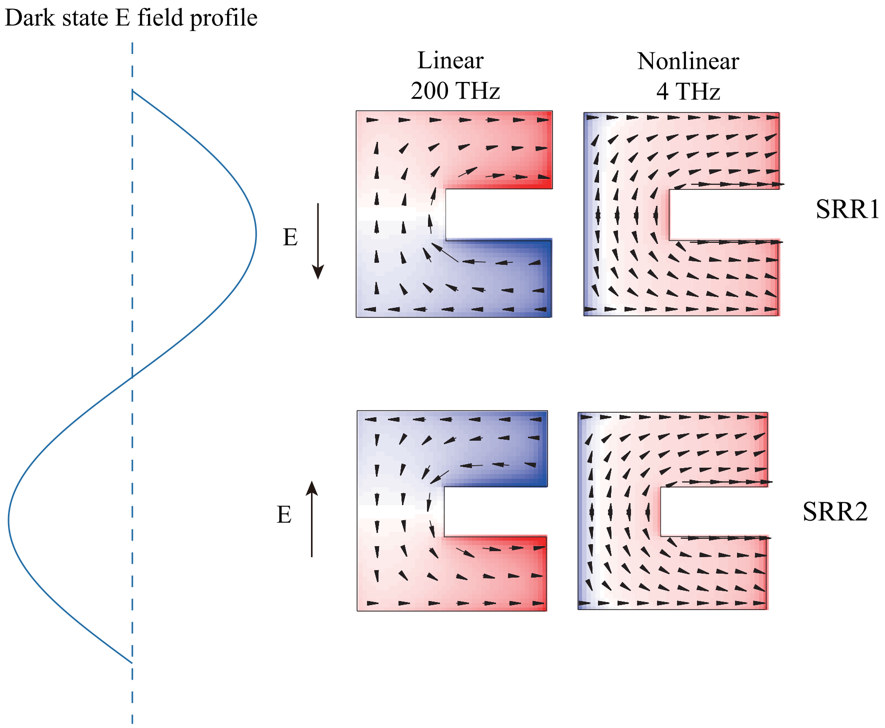

Figure S6. Current and charge density distributions in two SRRs at the frequency of linear response (200 THz) and THz generation (4 THz).

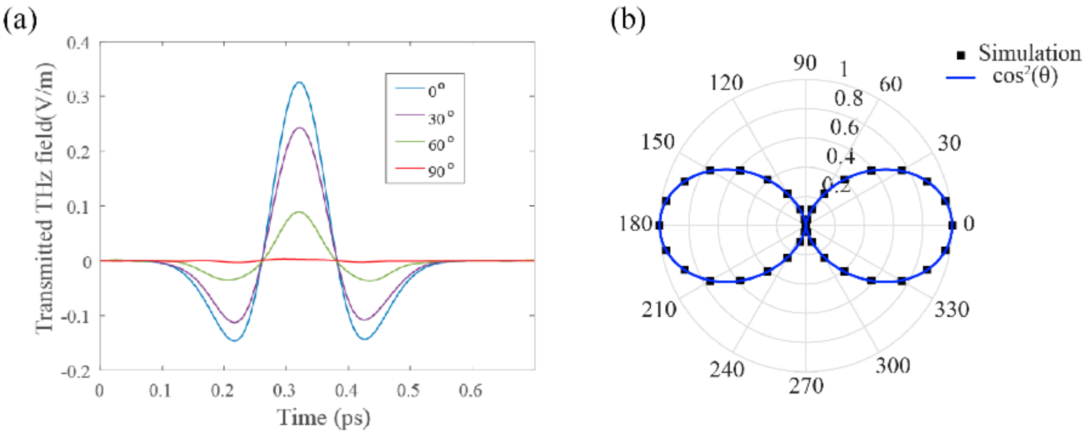

Figure S7. Polarization dependence of THz generation from our metasurface. (a) THz signals for different polarization angles. (b) Polar plot of the peak-to-peak amplitude of THz emission as a function of the polarization angle.

Figure S6 shows the fundamental magnetic dipole resonance of SRRs under normal incidence, excited by *y*-component of electric field. This circular linear current in the SRRs is critical for obtaining constructive interference of the THz generation. When the polarization of the incident wave is parallel to the gap of SRRs (along *y*-axis), the second-order nonlinear currents in both arms are parallel along x-axis and thus nonlinear radiation fields will be observed in the far field. In contrast, when the polarization is perpendicular to the gap of SRRs (along *x*-axis), this ring current can be excited and the resulting second-order nonlinear currents in both arms of each are parallel along *x*-axis and thus nonlinear radiation fields will be observed in the far field. In contrast, when the polarization is perpendicular to the gap of SRRs (along *x*-axis), the excitation of a circular current is forbidden by symmetry and only straight-line linear currents are induced in the SRR arms. Then, the nonlinear currents in the two arms show reverse flow directions along *x*-axis, leading to the vanishing of radiation in the far field. Consequently, the proposed THz emitter indeed has polarization dependence. Figure S7(a) shows the time-domain THz electric field for four different polarization angles (defined between the direction of the incident electric field and the *y*-axis), i.e., 0°, 30°, 60° and 90°. Figure S7(b) shows the polar plot of the peak-to-peak amplitude of THz signals versus the polarization angle. We can see that the simulated results fit very well with $\cos^2(\theta)$, consistent with the polarization control for the second-harmonic generation from SRR metasurface reported in Ref. [34].